Journal of Materials Chemistry C

ROYAL SOCIETY OF CHEMISTRY

PAPER

View Article Online
View Journal | View Issue

Cite this: J. Mater. Chem. C, 2025, 13, 18894

Deep eutectic solvent infused silk fibroin gels for flexible touch sensing

Yu Fu,†[a] Liujingzhou Li,†[a] Chao Ye,†[b] Leitao Cao,[c] Jinrong Yao,[a] Xin Chen,[a] Shengjie Ling *[ad] and Zhengzhong Shao *[ae]

Received 22nd June 2025,
Accepted 13th August 2025

DOI: 10.1039/d5tc02405f

rsc.li/materials-c

Silk fibroin hydrogels offer attractive biocompatibility and optical clarity but suffer from water-induced fragility, freezing, and biofouling. Here, regenerated silk networks are enzymatically cross-linked and subsequently exchanged with choline-chloride deep eutectic solvents (DESs) containing glycerol and ethylene glycol to create transparent, ionically conductive SF-DES gels. DES infusion preserves the protein's β-sheet framework while generating a more homogeneous nanonetwork and denser microstructure, increasing compressive modulus by up to 70% without altering protein concentration. The low volatility and depressed freezing points of DESs impart exceptional durability: the glycerol-based gel loses <5% mass under 37 °C, RH 35% airflow for 7 days, remains unfrozen at −80 °C, and the ethylene glycol-based gel maintains flexibility and conductivity of 0.013 mS cm^{-1} at −40 °C. Choline-based electrolytes inhibit growth of *Escherichia coli* and *Staphylococcus aureus*, mitigating microbial degradation. Leveraging this combination of mechanical resilience, environmental stability, ionic conductivity, and antimicrobial activity, bendable indium-free capacitive touch sensors are fabricated that achieve centimeter-scale position resolution and rapid gesture tracking. The study establishes DES infiltration as a general, aqueous-compatible route to robust, multifunctional protein gels, opening opportunities for sustainable wearable electronics, biomedical interfaces, and extreme-environment sensing.

Introduction

Hydrogels derived from natural proteins have attracted sustained interest due to their combination of softness, biocompatibility, mechanical robustness, and versatile functionality. Among protein-based hydrogels, regenerated silk fibroin (SF) stands out for its exceptional mechanical properties,[1–3] optical transparency,[4] mild aqueous processing conditions,[5] and inherent biocompatibility.[6,7] These attributes have made SF hydrogels promising candidates for bioelectronics, soft robotics, tissue engineering, and wearable electronic devices. Nevertheless, conventional SF hydrogels are typically prepared from aqueous solutions and thus contain a high water content, resulting in limited environmental stability, poor antifreeze properties, susceptibility to microbial contamination, and mechanical brittleness upon drying or exposure to sub-zero temperatures. Such intrinsic limitations severely restrict their practical deployment in fluctuating environmental conditions and demanding application scenarios, including flexible electronics, sensors, and implantable devices.[8–10]

To overcome these intrinsic challenges, recent studies have explored solvent replacement strategies,[11–13] aiming to replace volatile and easily frozen water molecules within hydrogels with stable, non-volatile solvents. Among these candidates, deep eutectic solvents (DESs) have emerged as a particularly attractive choice. DESs, formed by the complexation between hydrogen bond acceptors and donors, exhibit unique physicochemical properties, including low volatility, negligible freezing points, adjustable ionic conductivity, and intrinsic antimicrobial activity.[14–17] These features enable DES-based gels to maintain excellent stability across wide temperature ranges and diverse environmental conditions. Although DES incorporation has been demonstrated in synthetic polymer gels, resulting in enhanced mechanical flexibility, antifreeze performance, and ionic conductivity,[18–23] systematic investigation of DES integration into protein-based gels remains largely unexplored. Consequently, critical questions regarding how DESs interact with protein networks, influence the hierarchical gel structure, and modulate overall material performance remain unanswered.

[a] State Key Laboratory of Molecular Engineering of Polymers, Department of Macromolecular Science, Fudan University, Shanghai 200433, China. E-mail: lingshengjie@fudan.edu.cn, zzshao@fudan.edu.cn
[b] School of Textile and Clothing, Yancheng Institute of Technology, Yancheng, Jiangsu 224051, China
[c] School of Physical Science and Technology, ShanghaiTech University, Shanghai 201210, China
[d] Department of Orthodontics, Multidisciplinary Consultant Centre, Shanghai Stomatological Hospital & School of Stomatology, Fudan University, Shanghai 200433, China
[e] Laboratory of Advanced Materials, Fudan University, Shanghai 200433, China
† The first three authors contributed equally.

Here, we present a two-step route to silk fibroin-deep eutectic solvent hybrids (SF-DES gels). Regenerated silk is first enzymatically cross-linked, then water is replaced with choline-chloride DESs containing glycerol, ethylene glycol, urea, or oxalic acid, yielding transparent, ionically conductive gels designated as SF-DES-CC/Gl (abbreviated SDCG), SF-DES-CC/EG (SDCE), SF-DES-CC/Ur (SDCU), and SF-DES-CC/OA (SDCO). Systematic comparison shows that DES infusion markedly increases compressive modulus—most prominently in SDCG and SDCE—while preserving the protein's β-sheet framework. Infrared, SAXS, and SEM analyses reveal that DESs generate a more open yet denser hierarchical network that underpins this mechanical reinforcement. The low volatility and depressed freezing points of DESs impart exceptional durability: SDCG loses $<5\%$ mass under hot, dry airflow, remains unfrozen at -80 °C, and SDCE retains flexibility and conductivity (0.013 mS cm^{-1} at -40 °C). Choline-based electrolytes also suppress *Escherichia coli* (*E. coli*) and *Staphylococcus aureus* (*S. aureus*) growth, mitigating biofouling. Exploiting this unique combination of toughness, transparency, conductivity, antifreeze capability, and antimicrobial activity, we fabricate bendable, indium-free capacitive touch sensors that deliver centimeter-scale positional accuracy and rapid gesture tracking. These results establish DES infiltration as a general strategy for endowing protein gels with multifunctional robustness, charting a pathway toward sustainable, biocompatible materials for wearable electronics, biomedical interfaces, and extreme-environment sensing.

Results and discussion

Fabrication of DES-infused silk fibroin gels *via* enzymatic cross-linking and solvent exchange

The preparation of silk fibroin (SF)-based deep eutectic solvent (DES) gels involves three primary steps (Fig. 1a). The first step entails the formulation of DES, followed by the enzymatic cross-linking of regenerated acidic silk fibroin hydrogels (Acidic c-SF), and finally, the transformation into DES-infused SF gels *via* a solvent-exchange process. In this study, four types of DESs were formulated, each using choline chloride as the hydrogen bond acceptor. Choline chloride was selected not only for its biocompatibility and non-toxic nature, but also for its capacity to form conductive eutectic systems with a wide range of hydrogen bond donors.[24] As hydrogen bond donors, we selected four representative compounds—glycerol, ethylene glycol, urea, and oxalic acid—each known for their robust hydrogen bonding capabilities and effectiveness in DES formation.[24–26] These donors vary in their ability to form extensive hydrogen bond networks, which in turn influence the properties of the resulting gels. To facilitate comparison, the DESs were designated as DES-choline chloride/glycerol (DES-CC/Gl), DES-choline chloride/ethylene glycol (DES-CC/EG), DES-choline chloride/urea (DES-CC/Ur), and DES-choline chloride/oxalic acid (DES-CC/OA).

The enzymatically cross-linked regenerated silk fibroin hydrogels were prepared following a previously reported protocol.[27] In brief, raw silk was degummed, dissolved, and dialyzed, followed by concentration ***via*** osmotic dehydration using polyethylene glycol to obtain silk fibroin aqueous solutions with defined protein concentrations. The pH of the SF solution was adjusted to 5.5, after which horseradish peroxidase (HRP) and hydrogen peroxide were added to initiate the oxidative coupling of tyrosine residues, resulting in the formation of cross-linked SF hydrogels. This enzymatically cross-linked hydrogel is referred to as Acidic c-SF in this work.

The final step involved immersing the Acidic c-SF hydrogels in each of the four DESs. Driven by the concentration gradient between the internal aqueous environment of the gel and the external DES, a solvent exchange process occurred, whereby water diffused outward and the DES components permeated into the gel network. Upon completion of this exchange, four distinct DES-infused SF gels were obtained.

Among the four SF-DES gels, SDCG and SDCE were selected for further in-depth experiments as they showed satisfactory performance in both the preliminary electrical conductivity tests (Fig. 1c) and the compressive mechanical tests (Fig. 1f and g). The compressive moduli of SDCG and SDCE were more than an order of magnitude higher than that of SDCU and SDCO, and their electrical conductivity was all in line with the needs of the application scenario. It should be noted that SDCO, although having the highest ionic conductivity, has poorer mechanical properties and stability due to severe protein degradation in the acidic solvent (pH = 2).

Multi-scale structural origins of enhanced compressive modulus in SF-DES gels

Comparison among the four types of SF-DES gels revealed that the compressive modulus of the gels increased following solvent exchange, with the SDCE and SDCG systems showing particularly pronounced enhancement (Fig. 1f and g). Given that the protein concentration remained consistent between SDCE, SDCG, and the original Acidic c-SF gels, this mechanical reinforcement is attributed to differences in the interactions between DES components and silk fibroin molecules ***versus*** those between water and silk fibroin during the solvent exchange process and within the final gel environment. To investigate the structural origins of the enhanced mechanical properties in SDCE and SDCG, we conducted infrared (IR) spectroscopy analysis. To minimize the effect of SF concentration on gel performance, we prepared all samples at 3 wt% SF. For additional comparison and to dissect the structure–property relationship in DES gels, we also prepared enzymatically cross-linked silk fibroin gels ***via*** solvent exchange using ethanol, ethylene glycol, and glycerol, respectively. These gels were denoted as SF-Et, SF-EG, and SF-Gl.

All five gels displayed characteristic IR spectra dominated by β-sheet conformations (Fig. 2a), evidenced by prominent absorption bands near 1620 cm^{-1}, corresponding to the amide I bands of β-sheet structures.[28,29] The conformation changes of SF at different time points during the solvent exchange process were characterized by performing ***in situ*** ATR-FTIR characterization of the gels (Fig. S3), demonstrating that we can

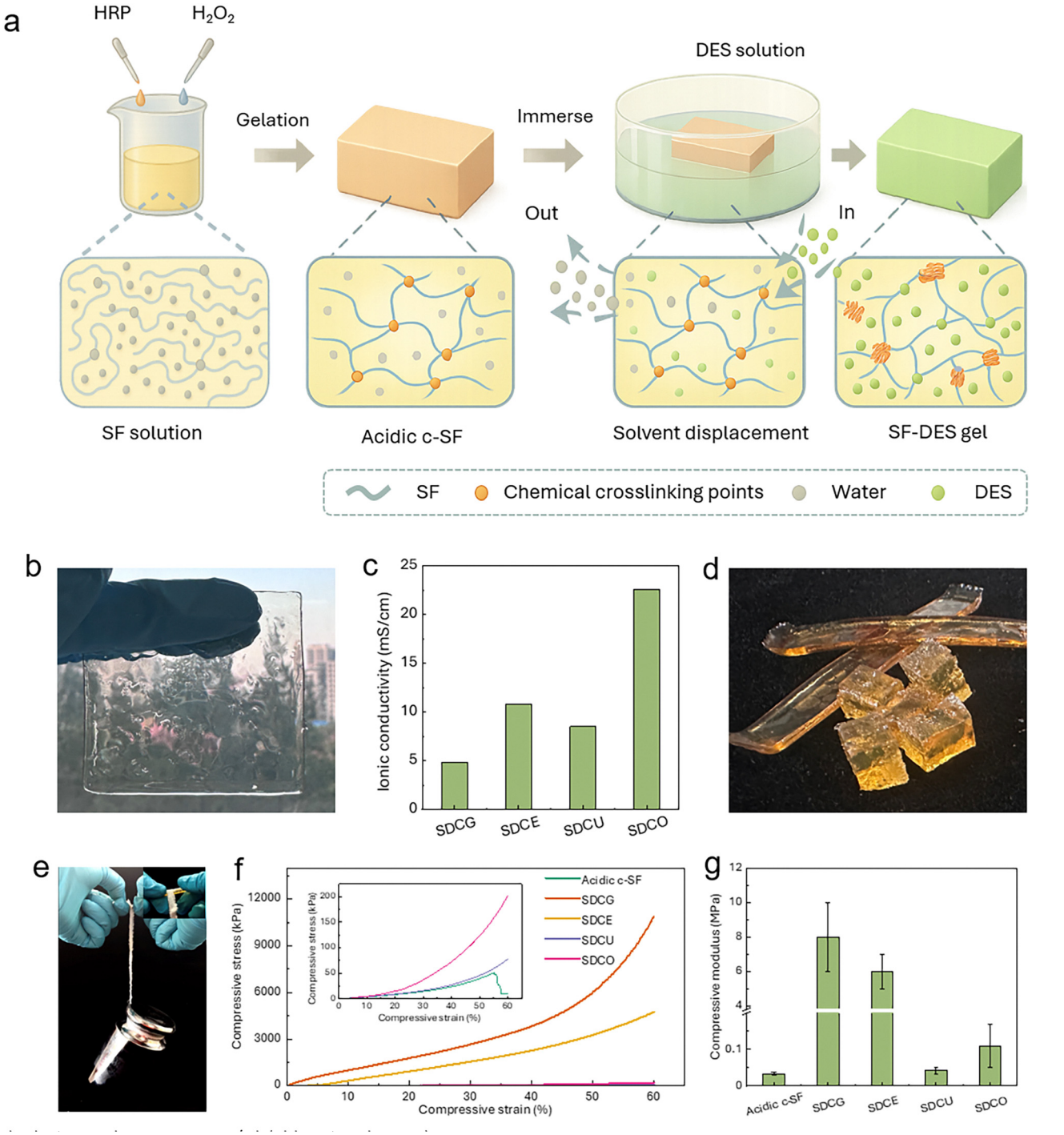

Fig. 1 Preparation of the SF-DES gels and mechanical characterization. (a) Schematic illustration of the SF-DES gel preparation steps. (b) Digital photo of SDCG. (c) Ionic conductivity of the SF-DES gels. (d) Digital photo of the SF-DES gels moulded into different shapes. (e) 1.5 g of SDCG can carry a weight of 2 kg. (f) Compressive stress–strain curves of Acidic c-SF and SF-DES gels. (g) Compressive modulus of the five gels.

qualitatively analyse the conformational changes (from random coil to β-sheet) in SF through FTIR even in the presence of the large amounts of DES. The similarity in the amide I spectral profiles among the different gel systems indicates that the secondary structures of the silk fibroin across these gels are largely conserved and predominantly β-sheet in nature. This structural consistency is essential for gel stability, as β-sheet domains serve as physical cross-linking points within the silk protein network. Their hydrophobic nature prevents water or other polar solvent molecules from penetrating the β-sheet regions, thereby contributing to the structural integrity of the gel. In contrast, gels rich in random coil structures are more susceptible to swelling or dissolution in aqueous or polar environments.

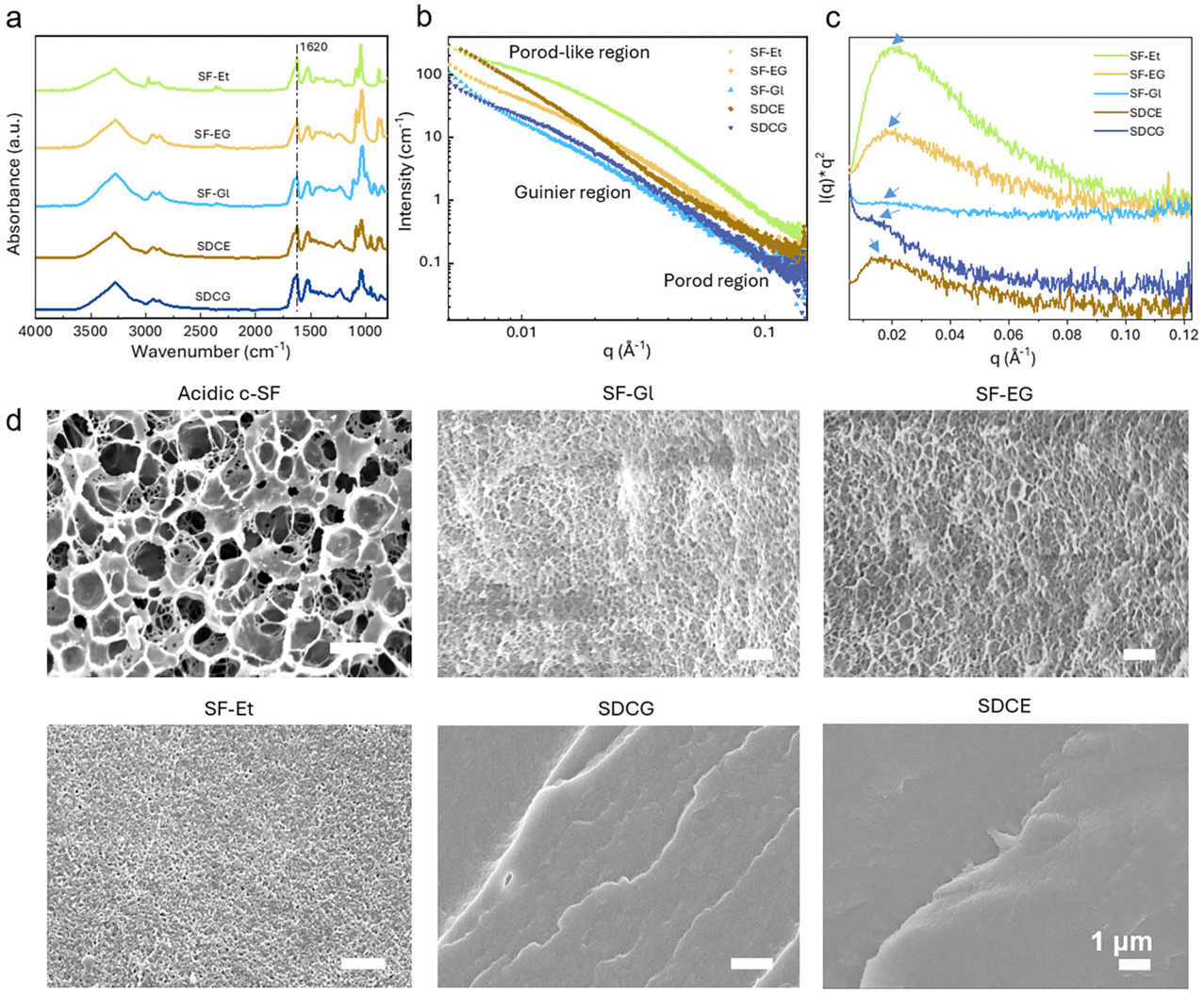

Fig. 2 Structural characterizations of the gels. (a) ATR spectra of the five gels. (b) SAXS curves and (c) Kratky plots of the five gels. (d) SEM images of the lyophilised gel samples; scale bars: 1 μm.

While no significant differences were detected in secondary structure among the gels, small-angle X-ray scattering (SAXS) was employed to probe nanoscale aggregation behavior (Fig. 2b and c). Compared to their corresponding alcohol-exchanged gels (SF-EG and SF-Gl), the DES gels (SDCE and SDCG) exhibited lower absolute slopes in the low-q Porod-like region, approaching a value of 2, and more defined peaks with leftward shifts in the Kratky plots. These features indicate the formation of more open (lower degree of aggregation) and uniform (more uniform scatterer size distribution) nanostructured networks in the DES gels, whereas the alcohol-based gels displayed larger, more heterogeneous aggregations.[30–32] These findings align with the hypothesis that DESs support extensive hydrogen bonding networks. Furthermore, scanning electron microscopy (SEM) images (Fig. 2d) demonstrated that alcohol-treated gels formed denser microporous structures, while DES-treated gels showed a smooth and compact morphology with minimal visible porosity.

Taken together, the enhancement in compressive modulus upon DES exchange results from the synergistic contributions of multi-scale structural features: the presence of hydrophobic β-sheet domains at the molecular level, the formation of a uniform hydrogen-bonded network at the nanoscale, and a denser microstructure at the microscale.

Environmental stability, antifreeze conductivity and antimicrobial performance of SF-DES gels

For applications such as capacitive touchscreens, the environmental stability of the gels is of particular importance. In this regard, DES-based gels offer distinct advantages due to the inherently low volatility and low freezing points of DES solvents under ambient conditions. These properties endow the gels with superior resistance to drying, excellent antifreeze capability, and enhanced thermal stability.

To evaluate the stability of the gels under different humidity conditions, SDCG and SDCE gels were subjected to a series of environmental exposures, including ambient conditions (room temperature, open air), RH 35% (37 °C with continuous hot-air flow), RH 11% (25 °C), RH 59% (25 °C), and RH 98% (25 °C).

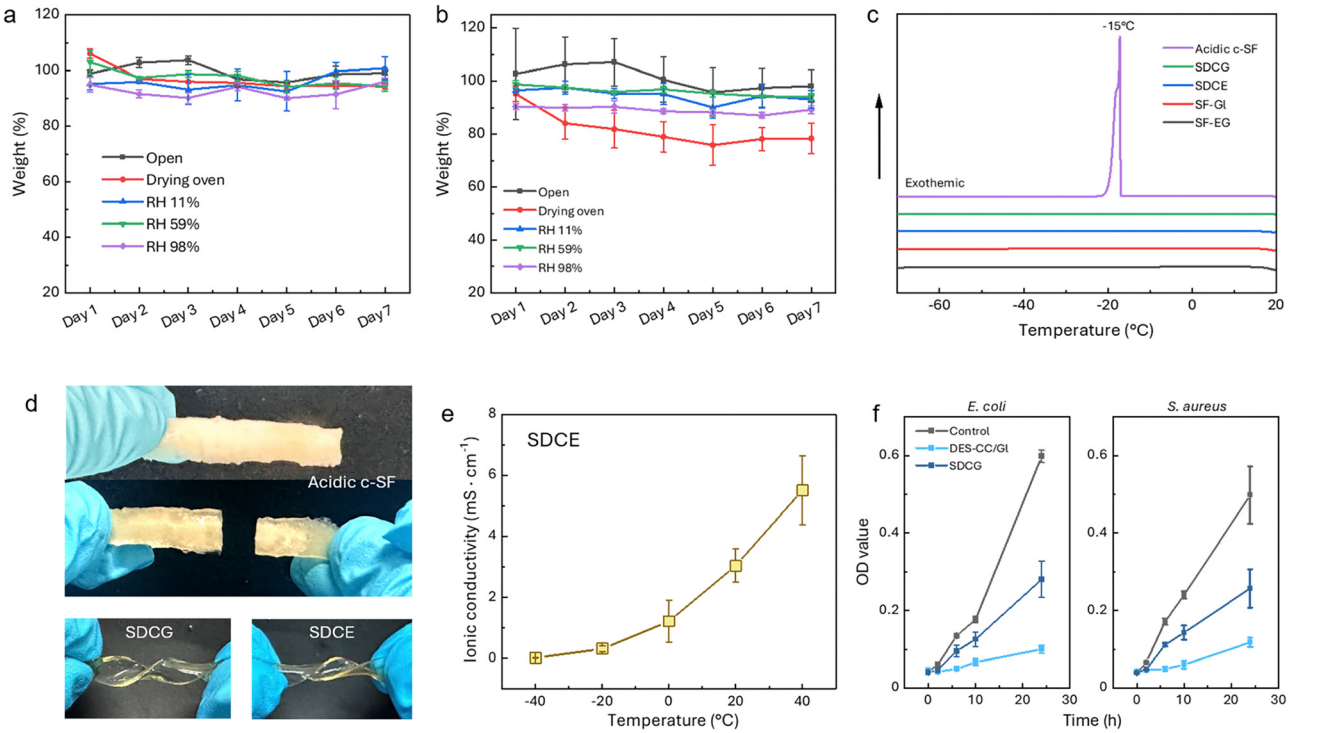

Fig. 3 Environmental stability of the SF-DES gels. Relative weight over time of (a) SDCG and (b) SDCE under different humidity conditions. (c) DSC curves of the five gels. (d) Digital photos of the gels placed at −20 °C for 1 month. (e) Ionic conductivity of SDCE measured at different temperature. (f) Bacterial growth rates when co-incubated with DES-CC/Gl and SDCG compared to control groups.

The mass change of the gels was monitored over time. As shown in Fig. 3a and b, both SDCG and SDCE demonstrated excellent environmental stability across all tested conditions. Even under the relatively harsh condition of RH 35% with 37 °C continuous hot-air exposure for 7 days, the mass loss of SDCG was limited to only 5%. In comparison, SDCE exhibited greater sensitivity to environmental variations, with mass losses reaching 22% under RH 35% at 37 °C, but only 2% under ambient conditions. Notably, SDCG consistently maintained negligible mass changes across all tested environments over the 7-day period, with mass loss remaining below 10%, confirming its superior environmental robustness.

The antifreeze properties of the SF-DES gels were further investigated by differential scanning calorimetry (DSC) to determine their freezing points. As shown in Fig. 3c, the Acidic c-SF hydrogel containing deionized water exhibited a sharp exothermic peak near −15 °C, indicating the freezing of internal water. In contrast, both SDCG and SDCE gels displayed no exothermic freezing peaks even when cooled to −80 °C, suggesting that the DES components remained unfrozen under extreme subzero conditions. This remarkable antifreeze behavior is attributed to the formation of low-energy hydrogen bond networks between the DES components, which lower the chemical potential of the liquid phase and consequently depress the freezing point to much lower temperatures. After storage at −20 °C for one month, Acidic c-SF gels became brittle and lost both elasticity and flexibility, while the DES-based gels retained excellent flexibility and could be easily twisted and deformed without fracturing (Fig. 3d).

The retention of unfrozen solvent within the gel matrix allows the solvent molecules to interact preferentially with the silk fibroin chains, forming a solvation layer that weakens interchain interactions and acts as a plasticizer due to the higher mobility of solvent molecules compared to the macromolecular protein chains. Moreover, the ionic conductivity of the DES gels arises from the presence of free ions generated by the weakening of tightly bound ion pairs through hydrogen bonding within the DES. As a result, the mechanical compliance and conductivity of SF-DES gels are well maintained even under extreme subzero temperatures. Conductivity measurements on SDCE confirmed its ability to retain conductivity at low temperatures; for example, even at −40 °C, the conductivity remained at 0.013 ± 0.006 mS cm^{-1}. As temperature increased, ionic mobility improved, and at −20 °C the conductivity rose to 0.31 ± 0.08 mS cm^{-1}. Above 0 °C, the conductivity increased linearly with temperature (Fig. 3e).

For practical applications where the gels are exposed to environmental conditions, protein-based gels such as silk fibroin are often susceptible to microbial contamination from bacteria or fungi, even during cold storage, which can compromise their physical integrity and biofunctionality. However, as shown in Fig. 3f, SDCG exhibited potent antibacterial activity against common pathogens, including *E. coli* and *S. aureus*. Antibacterial assays demonstrated a significant reduction in bacterial growth rates when co-incubated with the SF-DES gels compared to control groups. This antibacterial effect was consistent with the strong inhibitory activity observed when DES

solvents were directly co-incubated with bacterial cultures, suggesting that the DES component plays a key role in imparting the antimicrobial properties to the SF-DES gels.

SDCE-based flexible touchscreen enables real-time position sensing and gesture tracking

Building on the advantages of silk fibroin-based deep eutectic solvent gels, particularly SDCE, in terms of transparency, mechanical properties, conductivity, and environmental stability, we further explored their potential application in flexible electronic devices, specifically touchscreens. Furthermore, by choosing touchscreen as our application and preparing thin film-like samples, we were able to effectively address the limitation of inhomogeneity in the solvent exchange method caused by factors such as sample size.

Surface capacitive touchscreen technology, due to its high sensitivity and low cost, has been widely adopted in daily life. However, most commercial touchscreens rely on rigid indium tin oxide (ITO) conductive glass substrates, which significantly limit their use in flexible and wearable electronics. The use of SDCE to construct touchscreens (referred to as SDCETS) offers a promising route to overcome these limitations.

Fig. 4a and b illustrate the structural schematic, circuit design, and touch positioning mechanism of the one-dimensional SDCETS. The SDCETS strip, with a length of L, is connected at both ends to platinum (Pt) electrodes and external resistors (R_e), which are further connected to an alternating current (AC) power supply with identical phase (6 kHz, ±0.6 V). Voltmeters V_L and V_R are connected across the sampling resistors to continuously record the voltage drops across R_e. Due to charge separation at the interface between the Pt electrodes and the electrolyte, an electrical double layer capacitance (C_{EDL}) is formed. When a finger or metal stylus contacts the SDCETS strip, a contact coupling capacitance (C_t) forms at the interface between the finger/stylus and the gel, allowing current to flow through the human body to ground. In this process, the SDCETS strip can be modeled as a virtual resistance (R_h), which is divided at the contact point into two portions proportional to the normalized distances α and $1-\alpha$, as shown in Fig. 4a.

The simplified equivalent circuit of the device is presented in Fig. 4b, where the two sections of the SDCETS strip, αR_h and $(1-\alpha)R_h$, form parallel branches, each in series with C_{EDL} and R_e. Since the AC frequency is sufficiently high, the voltage drop across C_{EDL} is negligible.[33,34] As the finger moves to the right, αR_h increases, reducing the current I_L through the left branch and consequently lowering the voltage U_L across R_e, while U_R increases accordingly. The touch position can thus be determined by the following relations:

$$1-\alpha \propto U_L \quad (1)$$

$$\alpha \propto U_R \quad (2)$$

Experimental verification is shown in Fig. 4c. A 10 cm × 2 cm SDCETS strip was divided into five touch positions, and a metal stylus was used to sequentially touch each point from $\alpha = 0.1$ to $\alpha = 0.9$ in 0.2 increments. Prior to contact, a stable baseline

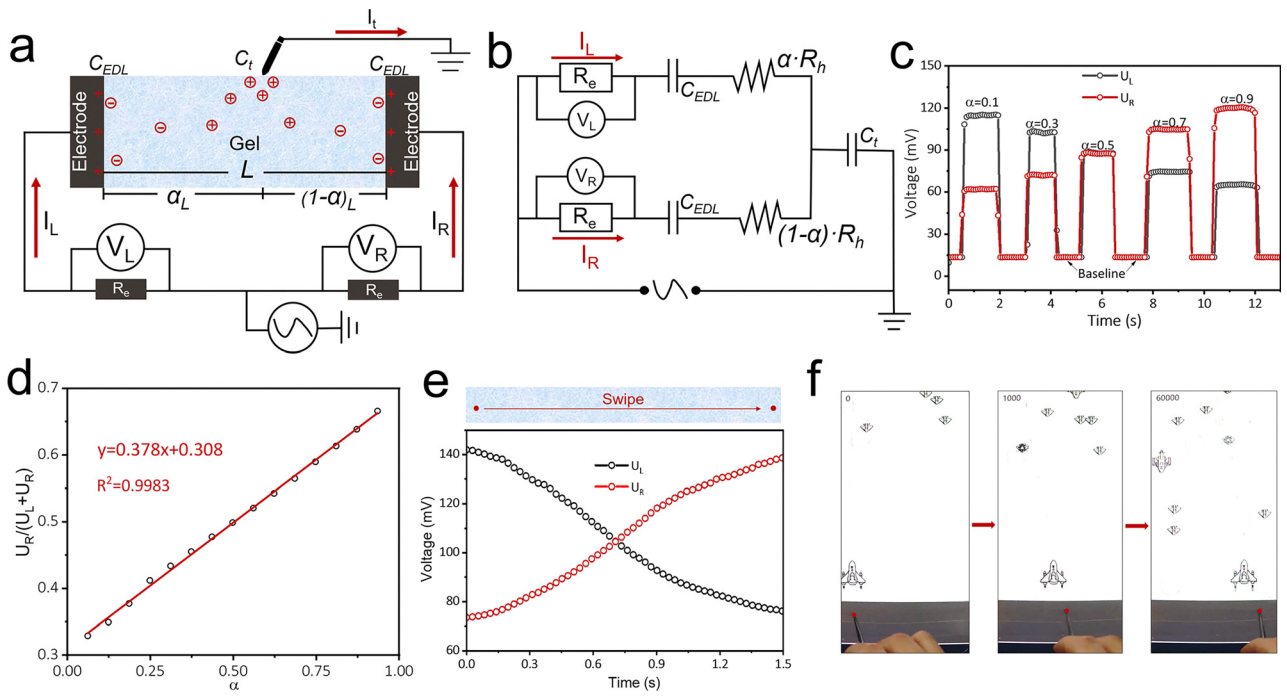

Fig. 4 Touch locating characteristics and application of the 1D SDCETS. (a) The architecture of 1D SDCETS touch strip. (b) The electrical circuit diagram of the SDCETS touch strip. (c) The recorded touching voltages (U_L and U_R) at different touch points (α = 0.1, 0.3, 0.5, 0.7, 0.9). (d) Plots of voltage ratio (U_L/U_R) *versus* proximity of touchpoint to the two Pt electrodes. (e) The recorded touching voltages (U_L and U_R) during swiping on the SDCETS with reading frequency of 30 Hz. (f) The SDCETS strip was used to play airplane battle game.

voltage (~13.5 mV) was observed due to constant leakage currents from the SDCETS to the environment.[35] Upon contact, additional touch voltages were immediately generated (*e.g.*, ~74 mV at α = 0.5), superimposed on the baseline. Both U_L and U_R exhibited sharp increases upon contact and returned to baseline upon release. As the contact point shifted from α = 0.1 to α = 0.9, U_L exhibited a linear decrease from 115 mV to 65 mV, while U_R showed a linear increase from 62 mV to 120 mV,

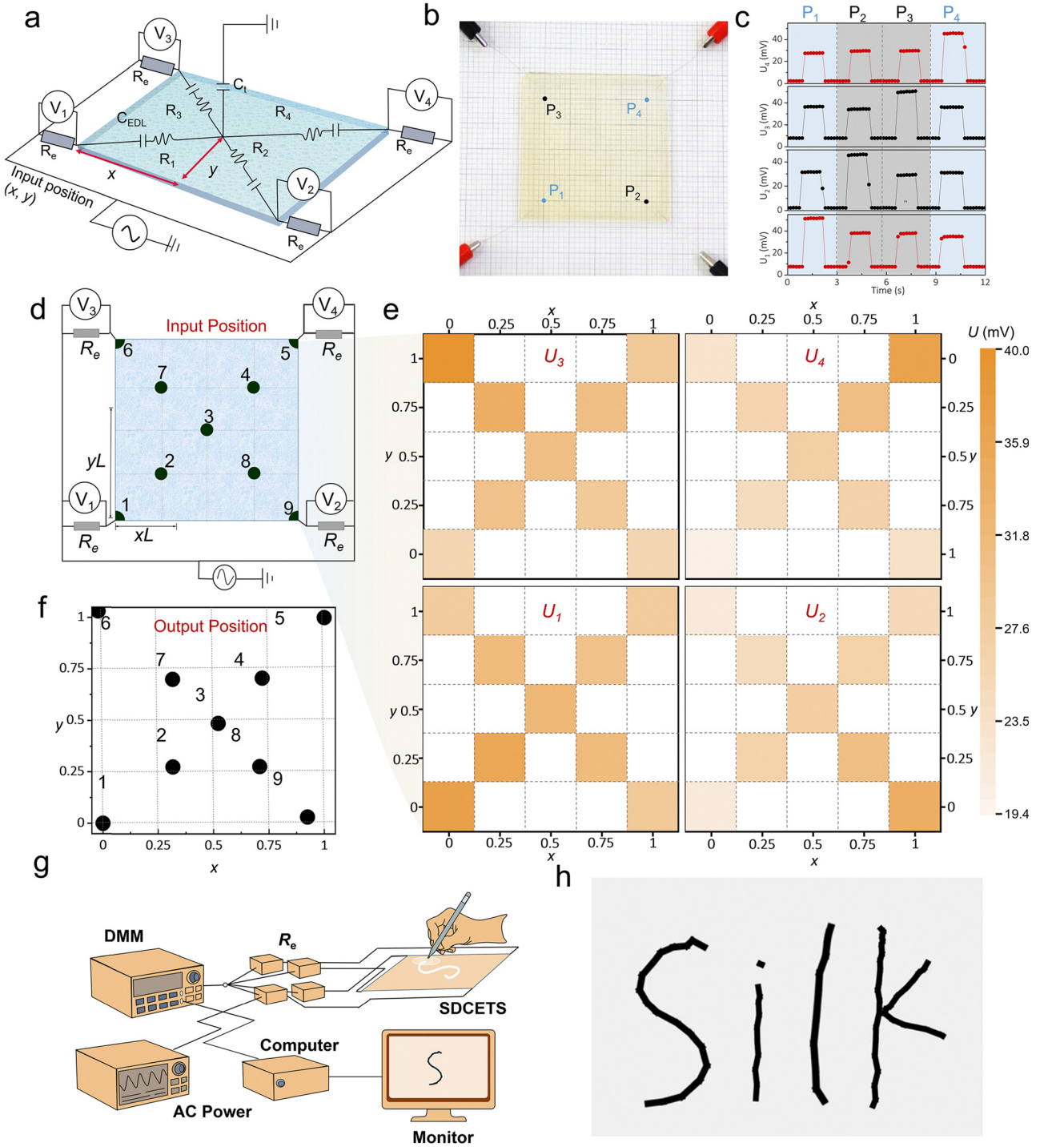

Fig. 5 Touch locating characteristics and application of the 2D SDCETS. (a) Touch locating characteristics and application of the 2D SDCETS. (b) A photograph of the SDCETS (6 cm × 6 cm × 1 mm) marked with four input positions (P_1–P_4). (c) The measured touching voltages (U_1 to U_4) during touching P_1–P_4 in sequence. (d) The SDCETS labeled with 9 input positions along the diagonal lines. (e) The heat map of touching voltages measured by four voltage meters (V_1–V_4) during touching points distributed evenly along diagonal lines. (f) The output points corresponding to the 9 input positions based on two-point positioning algorithm. (g) and (h) Schematic of the real-time drawing system based on SDCETS (g) and characters "silk" written through it (h).

consistent with the theoretical relationships described above, confirming the capability of SDCETS to perceive touch positions based on voltage changes.

To assess the precision of touch positioning, a 16 cm × 2 cm SDCETS strip was divided into 15 touch points spaced 1 cm apart. The responses of U_L and U_R at each position are shown in Fig. S4. Calculation of $U_R/(U_L + U_R)$ at each point revealed a clear linear relationship with touch position, indicating that a simple two-point calibration is sufficient to achieve accurate touch localization using SDCETS.

The response sensitivity of the SDCETS was further evaluated at various data acquisition frequencies. Owing to the high AC frequency, touch signals could be clearly detected at sampling rates of 3 Hz, 30 Hz, and 300 Hz without compromising sensitivity. The response times were measured as 677 ms, 68 ms, and 16 ms, respectively, enabling adjustable sensing speeds for different application scenarios (Fig. S5), For example, the SDCETS strip could be used as a virtual piano keyboard to play piano game (Fig. S6).

Beyond discrete touch point localization, SDCETS also enables continuous tracking of finger movements along the strip. During continuous sliding from left to right along a 10 cm strip, U_L steadily decreased while U_R increased, with faster response rates observed at higher sampling frequencies (Fig. 4e and Fig. S7). This demonstrates that SDCETS can capture sliding gestures, which may be useful for controlling virtual characters or navigating obstacles in gaming or robotic applications (Fig. 4f).

Expanding the design, we fabricated a two-dimensional (2D) SDCETS capable of real-time touch localization. The screen was constructed using a similar circuit and device design to the 1D strip (Fig. 5a). Four corners of the square SDCETS film were connected to Pt electrodes, each linked in series with external resistors (R_e), and voltages at each resistor were monitored independently using voltmeters V_1, V_2, V_3, and V_4. Touch positions were represented by normalized coordinates x and y (Fig. 5a). Upon touch, the panel was divided into four resistive sectors, forming a parallel circuit analogous to the one-dimensional configuration (Fig. S8). As with the 1D device, the touch voltage correlated inversely with the distance between the touch point and the respective electrode. As shown in Fig. 5b, touching corner positions P_1–P_4 resulted in the highest voltage readings from the nearest electrode and the lowest from the farthest (Fig. 5c). For example, when touching P_1, V_1 recorded the highest voltage while V_4 recorded the lowest.

To systematically evaluate the touch localization accuracy, nine target points were sequentially touched along the diagonal of the SDCETS panel (Fig. 5d), and the corresponding voltages were recorded in Table S1. The heatmaps in Fig. 5e depict the measured voltages at each sensor for the various touch points. As the finger moved away from a given electrode, the corresponding voltage decreased (***e.g.***, U_1 decreased from 37.1 mV to 27.7 mV when moving from point 1 to point 5, and then increased to 31.1 mV at point 7). For each point, the measured voltages U_1, U_2, U_3, and U_4 were inversely proportional to their respective normalized diagonal distances from the electrodes, consistent with the geometric model shown in Fig. 5a.

The touch position (x, y) on the 2D panel was further calculated by approximating the 2D system as two independent 1D strips along horizontal and vertical axes. The following relations were used:

$$x \propto (U_2 + U_4)/(U_1 + U_2 + U_3 + U_4) \quad (3)$$

$$y \propto (U_3 + U_4)/(U_1 + U_2 + U_3 + U_4) \quad (4)$$

Using these expressions, the measured voltages U_1–U_4 for the nine touch points were converted to touch positions ***via*** a two-point calibration algorithm (Fig. 5f). Detailed calculations are provided in Note S1 and Table S1. The calculated output positions aligned well with the actual input positions (Fig. 5d), demonstrating the capability of SDCETS for accurate 2D touch localization.

As a demonstration, we developed a real-time drawing system using the SDCETS. A custom Python program recorded real-time voltage signals from the four electrodes during finger or metal stylus contact, calculated the corresponding x and y coordinates, and plotted the trajectories using pyQT to generate freehand sketches, exemplified by rendering the word ''SILK'' (Fig. 5g and h).

Conclusions

This study establishes an enzyme-cross-linking and solvent-exchange route that replaces water in regenerated silk fibroin hydrogels with choline-chloride deep eutectic solvents, yielding transparent and ionically conductive SF-DES gels. Systematic comparison of four hydrogen-bond donors shows that glycerol- and ethylene-glycol-based systems provide the greatest mechanical reinforcement, raising compressive modulus without altering -sheet content. Multi-scale structural analyses link this enhancement to a homogeneous nanonetwork nested within a densified microstructure. The non-volatile and low-freezing-point nature of the eutectic phase endows the gels with long-term resistance to drying, negligible mass loss under hot or humid air, and an ability to remain flexible and conductive to −80 °C. The intrinsic antimicrobial activity of choline-based electrolytes further suppresses bacterial colonization, addressing a critical vulnerability of protein gels in open environments. Leveraging these combined attributes, bendable, indium-free capacitive sensors fabricated from the glycerol system exhibit centimeter-scale positional accuracy, rapid gesture tracking, and stable performance across a broad temperature range. The results demonstrate that deep eutectic solvents provide a general, water-compatible strategy for imparting toughness, environmental robustness, ionic conductivity, and bioprotection to protein networks. Such multifunctional silk gels present an attractive, sustainable alternative to oxide-coated conductors for next-generation wearable electronics, biomedical interfaces, soft robotics, and sensing devices required to operate under mechanically demanding and harsh climatic conditions.

Experimental section

Preparation of deep eutectic solvents (DESs)

Choline chloride (Shanghai Aladdin Biochemical Technology Co., Ltd) was mixed with glycerol (Shanghai Aladdin Biochemical Technology Co., Ltd), ethylene glycol (Shanghai Aladdin Biochemical Technology Co., Ltd), urea (Shanghai Aladdin Biochemical Technology Co., Ltd), and oxalic acid (Shanghai Aladdin Biochemical Technology Co., Ltd) at molar ratios of 1 : 2, 1 : 2, 1 : 2 and 1 : 1 respectively. The mixtures were stirred and heated at 90 °C until uniform transparent solutions were obtained. After cooling to room temperature, deep eutectic solvents (DES-CC/Gl, DES-CC/EG, DES-CC/Ur and DES-CC/OA) were prepared.

Fabrication of DES-infused silk fibroin gels *via* enzymatic cross-linking and solvent exchange

Preparation of enzymatically cross-linked SF hydrogels. Enzymatically cross-linked SF hydrogels were prepared as previously reported. Raw silk was boiled in 0.5 wt% sodium carbonate (Na_2CO_3, Sinopharm Chemical Reagent Co., Ltd) solution for 45 minutes to remove sericin. The silk was then rinsed three times with deionized water and dried at 40 °C for 12 hours to obtain degummed silk. 10 g of degummed silk was dissolved in 100 mL of 9.3 mol L^{-1} lithium bromide (Shanghai Aladdin Biochemical Technology Co., Ltd) solution at 60 °C and stirred at 300 rpm for 1 hour. The solution was filtered through eight layers of gauze to remove insoluble impurities, and then dialyzed using a dialysis bag (14 000 Da molecular weight cutoff) against deionized water for 3 days to obtain regenerated silk fibroin solution. The SF solution was concentrated using 15 wt% polyethylene glycol (Sinopharm Chemical Reagent Co., Ltd) *via* reverse osmosis to achieve a certain protein concentration. The pH of the SF solution was adjusted to 5.5, then horseradish peroxidase (HRP) and hydrogen peroxide were added to initiate oxidative coupling of tyrosine residues, resulting in the formation of cross-linked SF hydrogel. This enzymatically cross-linked hydrogel is referred to as Acidic c-SF in this study.

Preparation of SF-DES gels. The Acidic c-SF gels were immersed in each of the four DESs for at least 3 days for thorough solvent exchange, yielding four distinct DES-infused SF gels. The volume of the DES solvent used for immersion was ten times the volume of the gel. The solvent used for immersion was replaced once every 24 hours to ensure adequate solvent exchange. Control samples (SF-Gl, SF-EG, and SF-Et) were prepared using the same procedure.

Mechanical and structural characterization of gels

Characterization of mechanical properties. Gels were cut into approximately 5 mm-sized cubes. The compressive mechanical properties were tested using an Instron 5565 universal testing machine (Instron, USA) at a compression rate of 5 mm min^{-1}, with at least three samples per group.

Fourier transform infrared (FTIR) spectroscopy. Surface chemical structures of the gel samples were characterized *in situ* using a Nexus 470 FTIR spectrometer (Nicolet, US). A tungsten lamp was used as the IR source. Spectral range: 4000–400 cm^{-1}, resolution: 4 cm^{-1}, number of scans: 64, scan rate: 0.2 cm s^{-1}. Measurements were performed with an ATR accessory, and the ATR crystal was cleaned with lint-free paper before use. Spectra were processed using the OMNIC software provided with the instrument for background subtraction and data smoothing. Polynomial fitting with six terms was applied.

Small-angle X-ray scattering (SAXS). The microstructure of the gel samples was characterized *in situ* using a Xeuss 2.0 SAXS instrument (Xenocs, France). Measurements were carried out in air. Film thickness: ~1 mm, incident wavelength: 1.54 Å (Cu Kα), scanning angle range: 0.1°–5°, step size: 0.01°, integration time: 1 s pt^{-1}, temperature: room temperature.

Fracture surface morphology. Fracture surface morphology of the gels was observed using an Ultra 55 scanning electron microscope (Zeiss, Germany) at an accelerating voltage of 3 kV. Samples were quenched in liquid nitrogen, freeze-dried, then fractured in liquid nitrogen, and gold-sputtered on the fractured surface before imaging.

Environmental stability tests

Stability of SF-DES gels under different humidity conditions. The gels were placed in environments with different humidity levels. Their mass was monitored over time to calculate the percentage change relative to the initial mass. Humidity environments at room temperature were created by placing saturated solutions of LiCl (RH 11%), NaBr (RH 59%), and K_2SO_4 (RH 98%) in desiccators. The 37 °C hot-air flow condition (RH ~35%) was achieved using a forced-air drying oven.

Low-temperature stability. Low-temperature stability of the gels was tested using a DSC 250 differential scanning calorimeter (TA Instruments, US). Samples (<10 mg) were sealed in aluminum pans, with empty pans as reference. Measurements were conducted under nitrogen protection (50 μL min^{-1}), equilibrated at 25 °C, then cooled to −80 °C at a rate of 5 °C min^{-1}.

Electrical conductivity. Electrical conductivity of the gels was measured using an electrochemical workstation (CHI660E, Shanghai Chenhua Instrument Co., Ltd). Gel samples (5 mm × 5 mm × 10 mm) were placed between two stainless steel electrodes, ensuring good contact. A.C. impedance measurements were performed in the frequency range of 0.01–10^6 Hz. After testing, Nyquist plots were obtained and the intersection with the X-axis was recorded as the gel resistance R.

Gel resistivity ρ was calculated using the following equation:

$$R = \rho L/S \quad (5)$$

where L is the gel thickness and S is the cross-sectional area.

Subsequently, gel conductivity σ was calculated using the following equation:

$$\sigma = 1/\rho \quad (6)$$

Temperature control was achieved using a climatic chamber (GD/HS6006, Shanghai Yuanang Instrument Co., Ltd). Before

testing, samples were equilibrated in the chamber for 30 minutes at the target temperature.

Bacterial culture. A total of 25 g of Luria-Bertani (LB) broth powder was dissolved in 1000 mL of deionized water and sterilized by autoclaving to prepare LB liquid medium. To prepare LB solid medium, 25 g of LB broth powder and 1.5% (w/v) agar were dissolved in 1000 mL of deionized water and sterilized by autoclaving. *Staphylococcus aureus* (*S. aureus*) and *Escherichia coli* (*E. coli*) were respectively inoculated onto LB agar plates and incubated at 37 °C. Frozen stocks of *S. aureus* and *E. coli* were resuspended in LB broth and incubated at 37 °C with shaking at 150 rpm for 24 h. Upon completion, the optical density at 600 nm (OD600) was measured using a UV-Vis spectrophotometer to determine bacterial concentration, which was subsequently adjusted to 1×10^6 colony-forming units per millilitre (CFU mL^{-1}) for downstream experiments. Undiluted bacterial suspensions were mixed with glycerol at a volume ratio of 7 : 3 and stored at −80 °C for long-term preservation.

Bacterial growth curve. A volume of 2 mL bacterial suspension (2×10^7 CFU mL^{-1} or 1×10^6 CFU mL^{-1}) was added to each well of a 24-well plate, followed by co-incubation with the test materials (DES solution or DES gel). Wells without added materials served as controls. The plates were further incubated, and samples were collected at 0, 2, 4, 6, 8, 10 and 12 hours. The absorbance at 600 nm (OD600) was measured to assess the inhibitory effect of the materials on bacterial growth over time. The absorbance of the bacterial suspension (Abs) was recorded, and relative bacterial viability was calculated as $Abs_{sample}/Abs_{control} \times 100\%$.

SDCE-based flexible touchscreen application

Preparation of the 1D and 2D SDCETS. To fabricate a 1D touch strip, each end of an SDCETS strip (10 × 2 × 0.1 cm, 16 × 2 × 0.1 cm) was connected to an external resistance (Re, 6.8 kΩ) by Pt wire. An AC power (DG1022Z, RIGOL) generated ±0.6 V, 6 kHz sine wave was connected to both Re. The voltage drop on each Re was collected through an independent channel in a desktop multimeter (DMM6500, Keithley) equipped with a multiplexer module (2000-Scan, Keithley). A software, Kickstart, was used to read the voltage signals by time. To fabricate a 2D touch screen, 4 corners of a square SDCETS (6 × 6 × 0.1 cm) were connected to a Pt wire, respectively, which was then connected to a Re (6.8 kΩ). The 4 Re were connected to the same AC power described above in parallel. The voltage on each Re was collected through the above-mentioned multimeter and software.

Coordinate positioning calculation and real-time drawing system based on SDCETS. Programs written in Python were used to simultaneously collect multi-channel touching voltages from the multimeter (DMM6500) equipped with a 2000-Scan multiplexer module and converted them into coordinate forms by the two-point positioning algorithm described in Note S1 and Table S1. After obtaining real-time touch coordinates, the pyQT module is used to implement the display of drawing strokes.

Author contributions

Y. F., C. Y., L. C., J. Y., X. C., S. L. and Z. S. contributed to the conceptualization of this work. Y. F. and C. Y. performed the experiments. Y. F., L. L., C. Y., S. L. and Z. S. analyzed the data. Y. F., L. L. and C. Y. wrote the initial manuscript. All authors reviewed and edited the manuscript. S. L. and Z. S. supervised the work and acquired funding.

Conflicts of interest

There are no conflicts to declare.

Data availability

The authors confirm that the data supporting the findings of this study are available within the article and/or its SI. The SI provides supplementary data on the gel components, conformation, and mechanical and electrical properties. See DOI: https://doi.org/10.1039/d5tc02405f

Acknowledgements

This work was supported by the National Natural Science Foundation of China (52322305, 52473098 and 52303158), the starting grant of Fudan University; The authors thank the staff members from BL01B and BL19U2 beamline of National Facility for Protein Science in Shanghai (NFPS) at Shanghai Synchrotron Radiation Facility, BL06B, BL16B1 and BL13HB1 beamline of Shanghai Synchrotron Radiation Facility, BL01B beamline of National Synchrotron Radiation Laboratory in Hefei (NSRL) at University of Science and Technology of China, for assistance during data collection. No ethical approval was required for the experiments described in this article.

References

1 C. S. Kim, Y. J. Yang and S. Y. Bahn, *et al.*, *NPG Asia Mater.*, 2017, **9**, e391.
2 F. Chen, S. Lu and L. Zhu, *et al.*, *J. Mater. Chem. B*, 2019, **7**, 1708–1715.
3 N. R. Raia, B. P. Partlow and M. McGill, *et al.*, *Biomaterials*, 2017, **131**, 58–67.
4 D. Kuang, F. Jiang and F. Wu, *et al.*, *Int. J. Biol. Macromol.*, 2019, **134**, 838–845.
5 G. Cai, W. Zhao and T. Zhu, *et al.*, *Regen. Biomater.*, 2025, **12**, rbaf019.
6 H. Liu, S. G. Wise and J. Rnjak-Kovacina, *et al.*, *Biomaterials*, 2014, **35**, 5138–5147.
7 S. Kurosaki, H. Otsuka and M. Kunitomo, *et al.*, *J. Nippon Med. Sch.*, 1999, **66**, 41–44.
8 S. Cui, Y. Li and Z. Xu, *et al.*, *ACS Appl. Mater. Interfaces*, 2025, **17**, 8657–8669.
9 Y. Chen, W. Guo and N. Chen, *et al.*, *Sens. Actuators, A*, 2025, **383**, 116231.

10 Y. Chen, Z. Chang and Y. Liu, *et al.*, *Eur. Polym. J.*, 2024, **210**, 112992.
11 T. Shu, K. Zheng and Z. Zhang, *et al.*, *Biomacromolecules*, 2021, **22**, 1955–1965.
12 H. Sun, Y. Zhao and S. Jiao, *et al.*, *Adv. Funct. Mater.*, 2021, **31**, 2101696.
13 H. Zhang, N. Tang and X. Yu, *et al.*, *Adv. Funct. Mater.*, 2022, **32**, 2206305.
14 M. J. Panzer, *Mater. Adv.*, 2022, **3**, 7709–7725.
15 A. Nicolau, A. L. Mutch and S. C. Thickett, *Macromol. Rapid Commun.*, 2024, **45**, 2400405.
16 S. E. Hooshmand, S. Kumar and I. Bahadur, *et al.*, *J. Mol. Liq.*, 2023, **371**, 121013.
17 Y. Nie, Y. Zhou and Y. Zhang, *et al.*, *Adv. Funct. Mater.*, 2025, **35**, 2418957.
18 C.-W. Lai and S.-S. Yu, *ACS Appl. Mater. Interfaces*, 2020, **12**, 34235–34244.
19 Y. Wang, Y. Zhang and J. Su, *et al.*, *ACS Sustainable Chem. Eng.*, 2020, **8**, 14243–14252.
20 B. Zhang, H. Sun and Y. Huang, *et al.*, *Chem. Eng. J.*, 2021, **425**, 131518.
21 Z. Li, X. Xu and Z. Jiang, *et al.*, *ACS Appl. Mater. Interfaces*, 2022, **14**, 44821–44831.
22 H. Qin, R. E. Owyeung and S. R. Sonkusale, *et al.*, *J. Mater. Chem. C*, 2019, **7**, 601–608.
23 R. Liu, C. Qiao and Q. Liu, *et al.*, *ACS Appl. Polym. Mater.*, 2023, **5**, 4546–4553.
24 Y. Guo, Y. Wang and H. Chen, *et al.*, *Carbohydr. Polym.*, 2022, **296**, 119939.
25 A. P. Abbott, G. Capper and S. Gray, *ChemPhysChem*, 2006, **7**, 803–806.
26 Y. Wang, J. Wang and Z. Ma, *et al.*, *ACS Appl. Mater. Interfaces*, 2021, **13**, 54409–54416.
27 Y. Fu, Q. Lin and R. Lan, *et al.*, *Small*, 2024, **20**, 2403376.
28 G. Carissimi, C. M. Baronio and M. G. Montalbán, *et al.*, *Polymers*, 2020, **12**, 1294.
29 M. Müller, M. Wöltje and M. Hofmaier, *et al.*, *Langmuir*, 2024, **40**, 16731–16742.
30 G. Ochbaum and R. Bitton, *Self-Assem. Biomater.*, 2018, 291–304.
31 R. Balu, S. Reeder and R. Knott, *et al.*, *Langmuir*, 2018, **34**, 9238–9251.
32 J. L. Whittaker, R. Balu and R. Knott, *et al.*, *Int. J. Biol. Macromol.*, 2018, **114**, 998–1007.
33 C. Keplinger, J.-Y. Sun and C. C. Foo, *et al.*, *Science*, 2013, **341**, 984–987.
34 J. H. Cho, J. Lee and Y. Xia, *et al.*, *Nat. Mater.*, 2008, **7**, 900–906.
35 H. Haga, J. Yanase, Y. Kamon, *et al.*, *SID Symposium Digest of Technical Papers*, 2010, vol. 41, pp. 669–672.